

Large Eddy Simulation of the flow around a finite-length square cylinder with free-end slot suction

Hanfeng Wang^{1,2}, Lingwei Zeng¹, Md. Mahbub Alam³ and Wei Guo^{*1,2}

¹School of Civil Engineering, Central South University, Changsha, China

²National Engineering Laboratory for High-speed Railway Construction, Central South University, Changsha, China

³Institute for Turbulence-Noise-Vibration Interaction and Control, Harbin Institute of Technology (Shenzhen), Shenzhen, China

(Received October 22, 2019, Revised January 2, 2020, Accepted January 5, 2020)

Abstract. Large Eddy Simulation (LES) is used to study the effects of steady slot suction on the aerodynamic forces of and flow around a wall-mounted finite-length square cylinder. The aspect ratio H/d of the tested cylinder is 5, where H and d are the cylinder height and width, respectively. The Reynolds number based on free-stream oncoming flow velocity U_∞ and d is 2.78×10^4 . The suction slot locates near the leading edge of the free end, with a width of $0.025d$ and a length of $0.9d$. The suction coefficient $Q (= U_s/U_\infty)$ is varied as $Q = 0, 1$ and 3 , where U_s is the velocity at the entrance of the suction slot. It is found that the free-end steady slot suction can effectively suppress the aerodynamic forces of the model. The maximum reduction of aerodynamic forces occurs at $Q = 1$, with the time-mean drag, fluctuating drag, and fluctuating lift reduced by 3.75%, 19.08%, 40.91%, respectively. For $Q = 3$, all aerodynamic forces are still smaller than those for $Q = 0$ (uncontrolled case), but obviously higher than those for $Q = 1$. The involved control mechanism is successfully revealed, based on the comparison of the flow around cylinder free end and the near wake for the three tested Q values.

Keywords: aerodynamic forces; finite-length square cylinder; steady suction; flow control; LES

1. Introduction

Flow around wall-mounted finite-length cylinder (WMFLC) is frequently encountered in engineering applications, e.g., high-rise buildings, chimneys, etc. The flow around a WMFLC is highly three-dimensional (3D) and drastically different from that around a two-dimensional (2D) one (Park and Lee 2000, Sumner *et al.* 2004, Wang and Zhou 2009, Krajnovic 2011, Sattari *et al.* 2012, Kawai *et al.* 2012, Zheng and Alam 2017, Wang *et al.* 2017, Bai and Alam 2018, Sohankar *et al.* 2018a, 2018b, Bhatt and Alam 2018, Rastan *et al.* 2019, Derakhshandeh and Alam 2019). Particularly, the flow around a WMFLC is characterized by tip vortices or trailing vortices, spanwise vortices and possible base vortices (Wang and Zhou. 2006, Wang and Zhou. 2009, Kawai *et al.* 2012, Rastan *et al.* 2017). Tip and base vortices induce downwash and upwash flows, respectively, tending to weaken the periodic spanwise vortex shedding (Porteous *et al.* 2014, Wang *et al.* 2016). The base vortices and associated upwash flow depend on the boundary layer thickness on the wall where the cylinder is mounted. The base vortices enhance with increasing boundary layer thickness (Wang *et al.* 2006). The spanwise vortices depend largely on the cylinder aspect ratio H/d , where H and d are the height and width of the cylinder, respectively. The shedding of spanwise vortices is generally asymmetric, but when H/d falls below a critical

value, it becomes symmetric (Sakamoto and Arie 1983, Okamoto and Sunabashiri 1992, Pattenden *et al.* 2005). Sakamoto and Arie (1983) suggested that this critical value of H/d is 3.0 for a finite-length circular cylinder and 2.5 for a square one.

Based on time-averaged near wake velocity field, Tanaka and Murata (1999) calculated the mean vortex line for a finite-length circular cylinder with $H/d=1.25$ and 10. They found that the vortices from both sides of the cylinder are connected with each other near the free end, forming an arch-type structure. Wang and Zhou (2009) performed flow visualization in the spanwise and lateral planes simultaneously for the flow around a finite-length square cylinder with $H/d = 7$. From an instantaneous point of view, they found that the spanwise shear flow and free-end shear flow are also connected with each other and form the arch-type structure. Kawai *et al.* (2012) confirmed this observation using 3D stereoscopic PIV measurement in the near wake of a finite-length square cylinder with $H/d = 2.7$.

High-rise buildings can be considered as typical wall-mounted finite-length cylindrical structures. The wind-induced forces and associated vibrations are generally crucial for its design (Gu and Quan 2004, Quan and Gu 2012). Shape optimization is one of the most widely used measures to reduce the wind load and wind-induced vibration of high-rise buildings (Dutton 1990; Choi *et al.* 2008; Tanaka *et al.* 2012, Kim *et al.* 2015). Kim *et al.* (2015) investigated the wind load of a simplified high-rise building model with a regular polygonal section, e.g. triangular, square, pentagon, etc. The effects of both side number n and spanwise helix were studied. The overturning and torsional moments decrease with increasing n , but the

*Corresponding author, Ph.D. Associate Professor
E-mail: Guowei@csu.edu.cn

decrease becomes less pronounced when $n > 5$. Meanwhile, the effect of the helix in reducing the aerodynamic forces also becomes limited when $n > 5$.

Many investigations have been conducted on the effects of corner modification, e.g., corner recessing, chamfering and rounding, on a high-rise building with a square cross-section (Kawai 1998, Tanaka *et al.* 2012, Carassale *et al.* 2014 and Li *et al.* 2018, Shang *et al.* 2019, Zafar and Alam 2019). For a high-rise square building model with $H/d=8$, Li *et al.* (2018) found that if its corners are modified to chamfered ones, the fluctuating cross-stream base moment can be reduced by 37.5%. Some other modifications were also tested to reduce the wind load on high-rise buildings. Dutton (1990) found that through openings in the upper half of a high-rise building can significantly suppress its wind load and associated transverse wind-induced vibration. Xie (2014) reported that tapering or stepping along the height of a high-rise building can reduce its cross-wind aerodynamic responses. However, all these shape optimization methods have significant effects on the structural and architectural design of the buildings (Mooneghi and Kargarmoakhar 2016).

Active control is also applicable for manipulating the flow over cylindrical structures. Li *et al.* (2003) used both steady suction and blowing near the rear stagnation point of a circular cylinder and found that the suction and blowing can successfully suppress the vortex shedding from the cylinder. Steady suction near the spanwise leading edges of a square WMFLC with $H/d = 3.7$ can reduce its mean aerodynamic drag by about 74% and effectively suppress the flow separations on the side faces (Zheng and Zhang 2012). Moreover, Menicovich *et al.* (2014) experimentally investigated the aerodynamic performance of a high-rise building model when a steady tangential blowing is applied to the spanwise leading edge of the model. The mean drag and fluctuating lift are reduced by 14.2% and 6.1%, respectively for a blow ratio of 2, which is defined as the ratio of the mean tangential jet velocity to the oncoming flow velocity. Zhang *et al.* (2016) compared the effects of steady suction at different positions of a square high-rise building model with $H/d=6$. The identified that the suction at the side faces is more efficient than that at the leeward face in view of the aerodynamic force suppression. Moreover, the control effect becomes more remarkable when the suction holes get closer to the flow separation corners. Note that, the perturbations in the above-mentioned passive and active controls are arranged along the spanwise direction of the cylinder, which is essentially similar to that for 2D bluff bodies (Choi *et al.* 2008).

Some studies pointed out that free-end shear flow and spanwise shear flow around a WMFLC are connected to each other and form a closed arch type structure (Tanaka and Murata 1999, Wang and Zhou 2009, Kawai *et al.* 2012, Zhang *et al.* 2017). Therefore, it may be possible to control the entire near wake flow and associated aerodynamic forces by manipulating the free-end shear flow. Park and Lee (2004) experimentally investigated the influence of the free-end geometry on the near wake of a finite-length circular cylinder of $H/d = 6$. Compared to a flap flat tip, a hemispherical free end can significantly weaken regular

vortex shedding from the cylinder and reduce the reverse flow zone downstream of the cylinder. More recently, Wang *et al.* (2018) found that the aerodynamic forces on a square WMFLC with $H/d = 5$ can be significantly reduced by steady slot suction near its free-end leading edge. Its fluctuating lift is reduced by 45.5% with the suction ratio of 1, i.e., when the suction velocity at the slot equals the oncoming flow velocity. Although Wang *et al.* (2018) investigated the behaviors of the free-end shear flow using Cobra probe and smoke wire flow visualization for different suction ratios, the control mechanism was not well understood.

In this paper, Large Eddy Simulation (LES) is used to study the influence of free-end steady slot suction on the aerodynamic forces of and flow around a finite-length square cylinder with $H/d = 5$. The simulation results under three typical suction coefficients are compared in detail, especially the free-end shear flow. The control mechanism of the steady slot suction at the free end of a finite-length square cylinder is paid attention.

2. Numerical simulation

2.1 Numerical methods

LES disintegrates the turbulent vortices into large scale and small scale with a certain filter. According to Kolmogorov's theory, large-scale vortices depend on the cylinder geometry, which can be explicitly solved. On the other hand, the small-scale vortices are more universal, represented by sub-grid-scale (SGS) model (Chen *et al.* 2009).

The Navier-Stokes (N-S) equations of incompressible fluid are shown in Eq. (1), and the filtered N-S equations are shown in Eq. (2)

$$\frac{\partial u_i}{\partial t} + \frac{\partial}{\partial x_j} (u_i u_j) = -\frac{\partial p}{\partial x_i} + \frac{\partial}{\partial x_j} [\nu (\frac{\partial u_i}{\partial x_j} + \frac{\partial u_j}{\partial x_i})] \quad (1a)$$

$$\frac{\partial u_j}{\partial x_j} = 0 \quad (1b)$$

$$\frac{\partial \bar{u}_i}{\partial t} + \frac{\partial}{\partial x_j} (\bar{u}_i \bar{u}_j) = -\frac{1}{\rho} \frac{\partial \bar{p}}{\partial x_i} + \nu \frac{\partial^2 \bar{u}_i}{\partial x_j^2} - \frac{\partial \tau_{ij}}{\partial x_j} \quad (2a)$$

$$\frac{\partial \bar{u}_i}{\partial x_i} = 0 \quad (2b)$$

where ρ is the density of the fluid, ν is the kinematic viscosity coefficient of the fluid, \bar{u}_i and \bar{u}_j are the filtered velocity components along the corresponding Cartesian coordinates x_i and x_j , respectively ($i, j = 1, 2, \text{ and } 3$), \bar{p} is the pressure after filtering, τ_{ij} is the unsolved SGS turbulent stress, where $\tau_{ij} = \bar{u}_i \bar{u}_j - \bar{u}_i \bar{u}_j$. The anisotropic part of the SGS stress is represented by an eddy viscosity model.

$$\tau_{ij} - \frac{1}{3} \tau_{kk} \delta_{ij} = -2\nu_{sgs} \bar{S}_{ij} = -\nu_{sgs} (\frac{\partial \bar{u}_i}{\partial x_j} + \frac{\partial \bar{u}_j}{\partial x_i}) \quad (3)$$

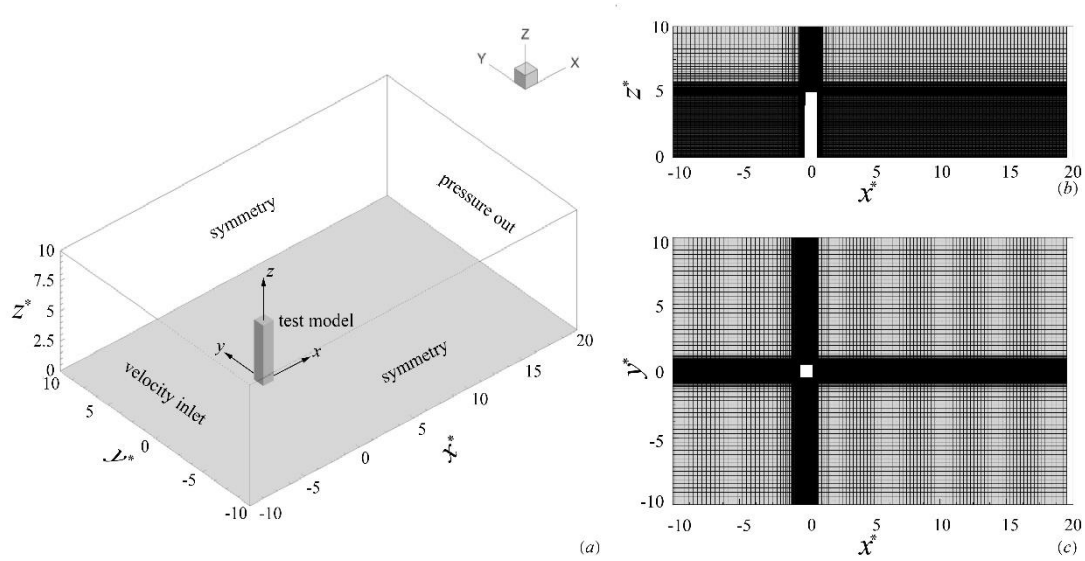


Fig. 1 Numerical simulation model and calculation mesh

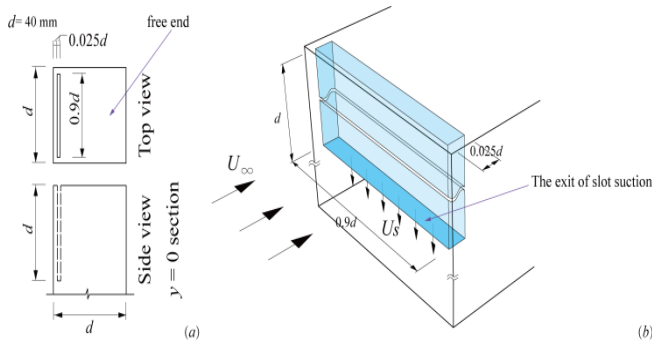


Fig. 2 Details of the suction slot

in which \bar{S}_{ij} is solvable scale strain rate tensor, τ_{kk} is the isotropic part of SGS stress and is included in the filtered pressure term, δ_{ij} is the normal stress of SGS, ν_{sgs} is sublattice turbulent eddy viscosity coefficient. Smagorinsky-Lilly hypothesis (Lilly 1992) is adopted in this paper, which suggests $\nu_{sgs} = (c_s \Delta)^2 |\bar{S}|$, where c_s is the Smagorinsky constant (Smagorinsky 1963), for flow around blunt bodies, $c_s = 0.1$ (Krajnovic and Davidson 2002). Tutar *et al.* (1998) have successfully demonstrated the feasibility of applying the Smagorinsky–Lilly SGS model to investigate flow past a circular cylinder in the subcritical flow regime. The strain rate tensor $\bar{S} = \sqrt{2\bar{S}_{ij}\bar{S}_{ij}}$. The Δ is the grid width, $\Delta = (\Delta x \Delta y \Delta z)^{1/3}$, where Δx , Δy , Δz are the grid size in x , y , and z directions, respectively. Commercial software ANSYS Fluent is utilized to conduct the numerical simulation.

2.2 Simulation model

The flow around a WMFLC with a square cross-section is simulated using LES. The width of the square cylinder $d = 40$ mm and its aspect ratio $H/d=5$, where H is the height

of the cylinder. The computational domain and coordinate system are shown in Fig. 1(a). The origin of the coordinates is defined at the center of the test model on the bottom wall. The length, width, and height of the computational domain are $30d$, $20d$, and $10d$, respectively. The model is $10d$ downstream from the inlet of the computational domain.

The slot for the steady suction is set at the cylinder free end, as shown in Fig. 2(a). The slot is $0.025d$ downstream from the free-end leading edge. The length and width of the suction slot are $0.9d$, $0.025d$, respectively, with a slot depth of d , as shown in Fig. 2(a). Note that, the boundary condition at the suction slot is not defined at the cylinder free end. Instead, a velocity outlet is defined at the bottom face of the slot, as indicated in Fig. 2(b). This definition of the approach for the suction slot allows the formation of secondary vortices near the entrance of the slot on the cylinder free end, which may have significant effects on the flow above the free end (Kotapati *et al.* 2007).

A uniform flow with the oncoming velocity $U_\infty=10$ m/s is given at the inlet of the computation domain. The Reynolds number Re , based on U_∞ and d , is 2.78×10^4 , which is the same as that used in Wang *et al.* (2018)'s experiment. The outlet of the domain is set as pressure-out. The top and side faces of the computational domain are defined as the symmetry boundary condition. Besides, the surfaces of the cylinder and the bottom wall of the computational domain are set as no-slip wall. The boundary layer thickness δ on the bottom wall is estimated to be about 10mm, i.e., $0.25d$, at the cylinder axis. That is, most of the cylinder span is immersed in uniform oncoming flow. The windward and leeward faces are named as A and C, and two side faces are named B and D.

Suction coefficient $Q = U_s/U_\infty$, where U_s is the velocity at the exit of the suction slot. Wang *et al.* (2018) investigated the effects of Q on the aerodynamic forces on a finite-length square cylinder with $H/d = 5$. They found that, compared to the uncontrolled case ($Q = 0$), the aerodynamic

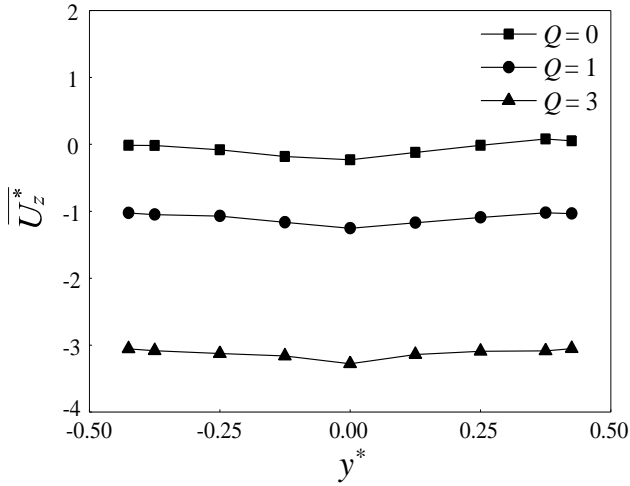


Fig. 3 Distributions of the suction velocity along the slot for different Q values

Table 1 Comparison of the three meshes used in the present LES

Case	Total grid number	Mesh number on model surface $N_x*N_y*N_z$	Δt	y^+
1	4×10^6	$41 \times 31 \times 61$	0.001	< 1
2	7×10^6	$45 \times 45 \times 151$	0.001	< 1
3	8×10^6	$50 \times 50 \times 151$	0.001	< 1

forces are minimum at $Q = 1$. The forces recover slightly with increasing Q for $Q \geq 1$ and become almost constant for $Q \geq 3$. Consequently, the present paper studies three typical suction ratios, i.e., $Q = 0, 1$ and 3 . To this end, the velocity at the exit of the suction slot (see Fig. 2(b)) is set as $U_s = 0, 10$ and 30 m/s, respectively.

The Strouhal number ($St = f_s \cdot d / U_\infty$, where f_s is the dominant vortex shedding frequency) of a square WMFLC with $H/d = 5$ is about 0.11 (McClellan and Sumner 2014, Unnikrishnan *et al.* 2018), slightly smaller than the corresponding value of a 2D square cylinder. Since $U_\infty = 10$ m/s, the dominant spanwise vortex shedding frequency is estimated to be 27.5 Hz, the corresponding period being 0.0364 s. The time step in the present simulation is set as 0.001 s, which is about 1/36 of the vortex shedding period.

Fig. 3 shows the distribution of the mean velocity $\overline{U_z^*}$ at the entrance of the suction slot for different Q . The superscript “*” in the present paper indicates normalization with U_∞ and/or d . For the uncontrolled case with $Q=0$, $\overline{U_z^*}$ is almost zero along the slot. The slight discrepancy from zero along the slot is ascribed to the effects of the slot cavity, as shown in Fig. 2(b). For $Q=1$ and 3 , $\overline{U_z^*}$ is also quite uniform along the slot, suggesting that the suction is approximately 2D at the entrance of the slot.

2.3 Mesh independence verification

The computational domain is discretized into structured hexahedral meshes, as shown in Fig. 1(b). The meshes at the slot are generated separately and are also discretized into structured hexahedral meshes. We defined the entrance

of the slot as interface 1, while the exit of the slot is defined as interface 2. Besides, a boundary layer meshes are produced at the entrance of the slot, the minimum grid size is 1×10^{-5} m with a ratio was 1.1. The mesh near the cylinder surface is refined in three directions. Three sets of meshes are tested to investigate their effects on the simulation results. Table 1 lists the information of the three sets of meshes, named Cases 1, 2, and 3, used for comparison. The total number of grids is about 4, 7 and 8 millions for the three cases. The main difference of these meshes lies in the number of the grids on the model surface in x, y and z directions, i.e., N_x, N_y and N_z , which are $41 \times 31 \times 61, 45 \times 45 \times 151$ and $50 \times 50 \times 151$ in Case 1, 2 and 3, respectively. All these three sets of meshes meet the condition of $y^+ < 1$ on the model surface. The main difference between them lies in the number of circumferential grids around the model.

Table 2 compares the results from the present simulations and those reported in the literature for square WMFLC. The St of the present simulation corresponds to that reported in the literature. For the three tested cases, the St increases very slightly from Case 1 to Case 3 by about 2.8%. For the time-averaged drag coefficient, $\overline{C_d}$ is the largest in Case 1. The overbar “ $\overline{\quad}$ ” means time-averaged value. It reduces by about 10% in Case 2 and keeps almost unchanged in Case 3. A relatively large discrepancy appears for the fluctuating drag coefficient C'_d . The C'_d being large in Case 1 reduces by about 35.5% and 62.7% in Cases 2 and 3, respectively. Though the percentages look big, the absolute differences in C'_d between the three cases are small. The fluctuating lift C'_l is also the largest in Case 1, decreasing by about 67.8% in Case 2 and keeping almost unchanged between Cases 2 and 3. The C'_l in Case 3 agrees well with the experimental result by wang *et al.* (2018). Considering all these comparisons, the mesh in Case 3 is adopted for the extensive simulations.

It is worth emphasizing that $\overline{C_d}$ of a WMFLC is closely linked to the wall boundary layer thickness δ . As shown in table 2, with δ ranging from $0.4 d$ to $3.5 d$, the experimental $\overline{C_d}$ changes from 1.29 to 1.62 (Sakamoto and Oiwake 1984, Sakamoto 1985, McClellan and Sumner 2014, Sumner and Ogunremi 2015, Unnikrishnan and Ogunremi 2017, Wang *et al.* 2017, Wang *et al.* 2018). The $\overline{C_d}$ from Case 3 accords well with the corresponding data from the experiments with smaller δ . Other experimental data with $H/d=4$ and 7 , which are close to the present investigated $H/d = 5$, are also given in table 2 for reference (Wang and Zhou 2009, Bourgeois *et al.* 2012, Saha 2013, Saedi *et al.* 2014, Rastan *et al.* 2017, Zhang *et al.* 2017).

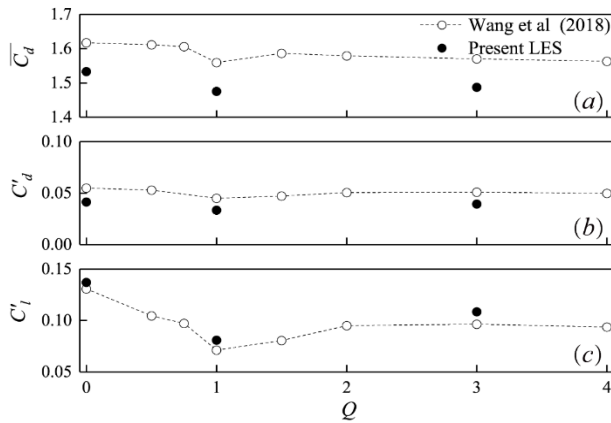
3. Results and discussions

3.1 Aerodynamic forces

Fig. 4 compares $\overline{C_d}$, C'_d and C'_l obtained from the present LES with the experimental results reported by Wang *et al.* (2018). The present C'_l is very close to the experimental results at all three typical Q . Since C'_l is directly related to the spanwise vortex shedding, this observation may indicate that the present LES can

Table 2 Comparison of simulated and experimental results

Cases	H/d	Re	δ/d	$\overline{C_d}$	C'_d	C'_l	St	Method
1 (4×10^6)	5	2.78×10^4	0.25	1.680	0.110	0.423	0.107	LES
2 (7×10^6)	5	2.78×10^4	0.25	1.503	0.071	0.136	0.109	LES
3 (8×10^6)	5	2.78×10^4	0.25	1.533	0.041	0.137	0.110	LES
Sakamoto and Oiwake (1984)	5	3.4×10^4	3.3	1.30	0.08	0.30	0.10	Exp
Sakamoto (1985)	5	$3.4 \times 10^4 \sim 1.7 \times 10^5$	3.5	1.29	0.082	0.31	0.10	Exp
Mcclean and Sumner (2014)	5	7.3×10^4	1.5	1.43	0.015	–	0.105	Exp
Sumner and Ogunremi (2015)	5	7.4×10^4	1.6	1.47	–	–	–	Exp
Unnikrishnan and Ogunremi (2017)	5	3.7×10^4	1.5	1.425	–	–	0.105	Exp
Wang <i>et al.</i> (2017)	5	6.8×10^4	1	1.51	–	–	0.11	Exp
Wang <i>et al.</i> (2018)	5	2.78×10^4	0.4	1.62	0.055	0.13	0.11	Exp
Bourgeois <i>et al.</i> (2012)	4	1.2×10^4	0.72	–	–	–	0.10	Exp
Saha (2013)	4	250	–	1.23	–	–	0.124	DNS
Saeedi <i>et al.</i> (2014)	4	1.2×10^4	–	–	–	–	0.106	DNS
Zhang <i>et al.</i> (2017)	4	1000	0.31	1.404	–	–	0.106	DNS
Wang and Zhou (2009)	7	9300	1.35	–	–	–	0.110	Exp
Rastan <i>et al.</i> (2017)	7	250	0.84	1.287	0.095	0.085	0.117	DNS

Fig. 4 Effects of suction ratio Q on $\overline{C_d}$, C'_d and C'_l

successfully extract the main features of spanwise vortex shedding. The present $\overline{C_d}$ and C'_d are slightly smaller than the experimental data. For example, at $Q = 0$, $\overline{C_d}$ is 1.53 in the present LES, approximately 5.5% smaller than that reported by Wang *et al.* (2018). The possible reason is that the boundary layer conditions in the present LES and the experiment are not completely identical. Particularly, the boundary layer thickness δ is $0.25d$ in the present LES and $0.4d$ in Wang *et al.* (2018)'s experiment. Although there are some quantitative differences in $\overline{C_d}$ and C'_d between the LES and experiment, their variations with Q have the same tendency. Both $\overline{C_d}$ and C'_d present their minimal values at $Q = 1$ and then recover a little bit at $Q = 3$. The maximal reduction in $\overline{C_d}$, C'_d , and C'_l are 3.75%, 19.08%, and 40.91%, respectively, compared to the uncontrolled case. These observations are similar to those reported by Wang *et al.* (2018), indicating the significant effects of the free-end suction on the aerodynamic forces on the square WMFLC.

Fig. 5 shows the instantaneous C_l at different Q , and the corresponding short-term Fourier analysis results along with power spectrum. The power spectrum provides time-

averaged spectral coefficients, which is useful to identify the dominant frequency in a signal and the strength of spectral peaks. For a non-stationary signal, a time-frequency plot is useful for understanding the flow physics (Alam *et al.* 2010). Time-frequency analysis using short-time Fourier transform (STFT) identifies the distribution of power as a function of the frequency at every instant for the signal analyzed. It is well known that, a large window size (signal length in time) improves the frequency resolution but reduces the temporal resolution, and vice versa. In the present STFT, Gaussian wind function is used. The width of the window is 0.1s to achieve a compromise between frequency and temporal resolutions.

As expected, for the uncontrolled case ($Q = 0$), the fluctuation in C_l is not stable over time. Both high- and low-amplitude fluctuations of C_l occur intermittently. This observation is consistent with that reported by Wang and Zhou (2009), Sattari *et al.* (2012) and Uffinger *et al.* (2013). The high-amplitude fluctuation of C_l corresponds alternate formation and shedding of spanwise vortices while the low-amplitude fluctuation is accompanied by co-existing spanwise vortices in the obstacle lee throughout the shedding circle (Bourgeois *et al.* 2011, 2012 and 2013). The shifting between these two typical shedding modes can be clearly observed in the time-frequency spectrum for $Q=0$ (Fig. 5(b)).

At $Q = 1$, the fluctuation in C_l significantly small compared to that at $Q = 0$ (Fig. 5(d)). Besides, the shifting between the two typical vortex shedding modes also becomes less obvious (Figs. 5(d), 5(e)). With the increase of Q to 3, both the fluctuation in C_l and the peak in its time-frequency spectrum enhance noticeably compared with those at $Q = 1$. For an easy comparison, the spectrum of C_l is normalized into dB scale using the peak value of $Q=0$ as reference. Obviously, the peak at $Q = 1$ is -5.05 dB, significantly lower than the zero at $Q = 0$. When Q is increased to 3, this peak value rises to -2.85 dB, albeit still

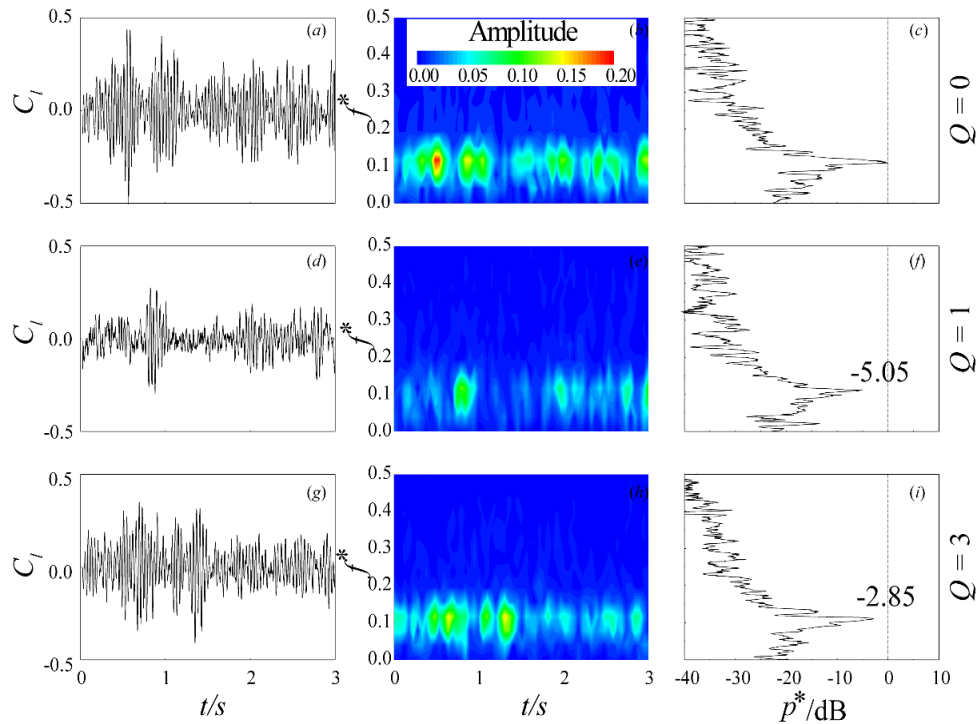


Fig. 5 Instantaneous lift, its short-term Fourier transform results, and power spectra for $Q=0, 1$ and 3

smaller than that for the uncontrolled case ($Q=0$) but higher than that for $Q=1$. This observation supports the Q effects on C'_l in Fig. 4.

Fig. 6 presents the distributions of the time-mean and fluctuating pressure coefficients \overline{C}_p and C'_p on the windward, side and leeward faces of the cylinder. The C_p and \overline{C}'_p are defined as $\overline{C}_p = 2(\overline{P} - p_\infty) / \rho U_\infty^2$ and $C'_p = 2P_{rms} / \rho U_\infty^2$, respectively, where \overline{P} is the time-averaged pressure, P_{rms} is the root-mean-square value of the fluctuating pressure, and P_∞ is the static pressure.

Distributions of \overline{C}_p and \overline{C}'_p on the side and leeward faces may reflect the vortex shedding behavior. Lee (1975) and Noda and Nakayama (2003) investigated the effects of oncoming flow turbulence on the aerodynamic characteristics of a 2D square cylinder, including the circumferential distribution of \overline{C}_p and \overline{C}'_p . They found that spanwise Karman vortex shedding is suppressed gradually with increasing turbulence intensity (Ti), especially for $Ti \geq 8\%$. The absolute values of both \overline{C}_p and \overline{C}'_p on the side and leeward faces decrease gradually, which is ascribed to the weakened spanwise vortex shedding.

As shown in figure 6, the distributions of \overline{C}_p and C'_p on the windward face are almost unchanged for the three typical Q values, except small \overline{C}_p appearing near the free-end leading edge for the controlled cases. For $Q=0$, the distributions of \overline{C}_p and C'_p on the side and leeward faces (i.e., B and C) change noticeably along the cylinder span, suggesting a strong three-dimensionality of the flow. The \overline{C}_p is relatively small near the trailing edge at the upper half of the cylinder (Fig. 6(b)). It gradually grows toward the base, apparently because of the effects of wall junction. This distribution concurs with that obtained experimentally

by Wang *et al.* (2017). The distribution of C'_p is mostly uniform near the cylinder midspan ($z^* \approx 1.5 - 3.5$). Note that, the values of \overline{C}_p and C'_p for the present finite-length square cylinder are far smaller than the corresponding values of a 2D square cylinder reported by Lee (1975), Noda and Nakayama (2003) and Wang *et al.* (2017). This is because the vortex shedding from a WMFLC is considerably weak, compared with that from a 2D cylinder.

For $Q=1$, the magnitudes of \overline{C}_p on faces B and C (Figs. 6(e) and 6(f) reduces slightly, compared with that for $Q=0$ (Figs. 6(b) and 6(c). Besides, C'_p the same faces (figure 6n, o) is considerably suppressed when compared with the $Q=0$ case (Figs. 6(k) and 6(i)). It indicates that the spanwise vortex shedding is considerably suppressed for $Q=1$. With Q increasing to 3, the suppression of \overline{C}_p and C'_p is less pronounced, which is consistent with the observations in Figs 4 and 5. It is worth mentioning that the effects of free-end suction appear not only on near the cylinder free end but also over the entire cylinder span (Fig. 6).

A special observation can be made at $Q=1$ with a close look at the \overline{C}_p distribution near the free end (Fig. 6(e)). The \overline{C}_p presents its minimum value of -1.0 on the side face near the cylinder free end, which is even lower than that at $Q=3$. It is interesting to figure out what happens on the cylinder free end at $Q=1$, which causes this local minimum \overline{C}_p near the cylinder free end and suppresses the aerodynamic forces most efficiently. As such, we look into the \overline{C}_p and C'_p distributions on the cylinder top surface (Fig. 7). Apparently, the distributions are highly contingent on Q . For $Q=0$, both \overline{C}_p and C'_p distributions are quite uniform, which can be ascribed to the fact that the free end is fully

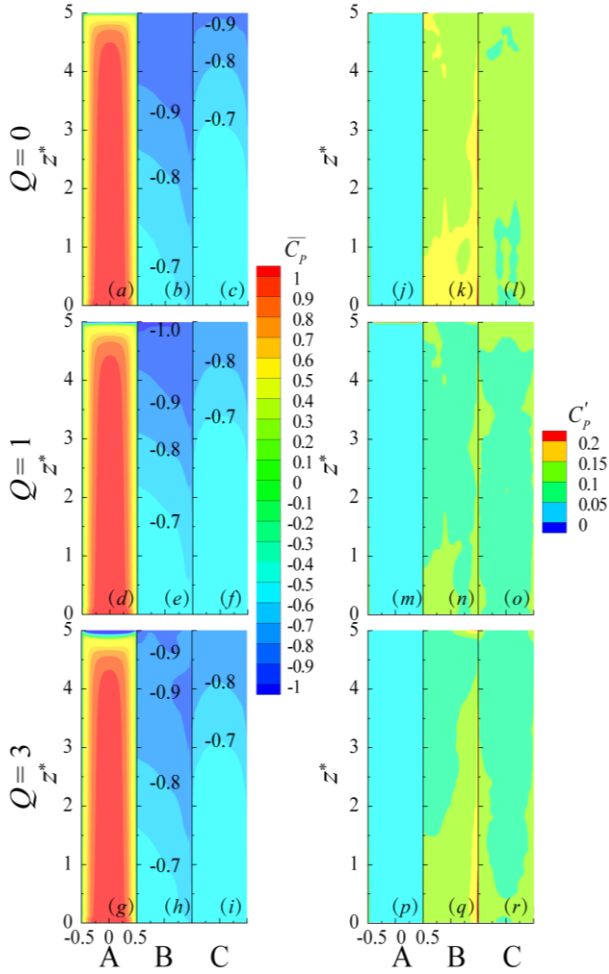


Fig. 6 Distributions of $\overline{C_p}$ and C_p' on the windward, side and leeward faces of the cylinder

immersed in the reverse flow formed by the free-end shear flow. The oncoming flow bends upward while approaching the cylinder free end, then separates from the leading edge forming a reverse flow on the free end (Sumner *et al.* 2017, Wang *et al.* 2018, Cao *et al.* 2019). From the direct numerical simulation (DNS) results, Rastan *et al.* (2017) found that the behavior of the free-end shear flow depends on the Reynolds number. The separated free-end shear flow reattaches on the free end at $Re \leq 40$ while remaining fully separated at $Re \geq 250$. The present $Re=2.78 \times 10^4$ nestles in the latter range; that is, the cylinder free end is expected to be completely immersed in the separated flow, which will be further confirmed later. The uniform distributions of $\overline{C_p}$ and C_p' thus prevail on the free end for $Q = 0$.

For $Q = 1$ and 3, the $\overline{C_p}$ and C_p' both vary on the free-end surface (Figs. 7(b), (e)). When $Q=1$, the $\overline{C_p}$ is small at the upstream half of the free end while large at downstream half. Meanwhile, remarkably high C_p' appears near the suction slot, with two tails extending to the downstream (Fig. 7(e)). For $Q = 3$, the $\overline{C_p}$ on the free end becomes uniform again, being significantly higher than that for $Q=0$. Interestingly, C_p' in most of the area downstream the suction slot is approximately zero, except at the side edges of the free end (Fig. 7(f)). The significant variations of $\overline{C_p}$ and C_p'

on the free end as well as of aerodynamic forces (Figs. 4 - 6) are obviously linked to the free-end slot suction. It is interesting to investigate the effects of slot suction on the free-end shear flow and to reveal its control mechanism.

3.2 Flow structures

3.2.1 Flow around the free end

The free-end shear flow is closely related to the downwash flow in the wake. Here, the effects of slot suction on the free-end shear flow are investigated. Figure 8 presents the time-averaged streamlines together with the distributions of turbulent kinetic energy TKE^* in the central symmetric plane at $y^* = 0$. The TKE^* is defined as $TKE^* = 0.5 \cdot (\overline{u_x'^2} + \overline{u_y'^2} + \overline{u_z'^2}) / U_\infty^2$, where $\overline{u_x'^2}$, $\overline{u_y'^2}$, $\overline{u_z'^2}$ are the variances of the velocity components in x , y and z directions, respectively. The time-averaged streamlines, shown in Figs. 8(a) - 8(c), are overlapped with the contours of mean streamwise velocity $\overline{U_x^*}$ for an easy interpretation. The red solid line and 'x' in Figs. 8(a) - 8(c) indicate the boundary of flow reversal ($\overline{U_x^*} = 0$) and the saddle point formed by the downwash and upwash flow (Wang *et al.* 2006), respectively.

At $Q = 0$, the streamlines separate from the leading edge of the free end and bend down in the near wake, forming a large recirculation zone, which is qualitatively similar to the PIV measurement results by Sumner *et al.* (2017). The streamwise length of the recirculation grows from the cylinder tip to the cylinder midspan, not varying much from the midspan to the base. It is maximum of $3.43d$ at $z^* \approx 2$. The downwash being much stronger than the upwash pushes the saddle point to be very close ($z^* = 0.40$) to the base (Fig. 8(a)). Wang and Zhou (2009) and Sumner *et al.* (2017) for a square WMFLC with the same H/d identified the saddle point at $z^* = 3.21$ and 2.86, respectively, which are higher than the present one. This is because the wall boundary layer in the present investigation is relatively thin, thus generating a weakened upwash flow in the near wake (Wang *et al.* 2006). The maximum TKE^* appears in the near wake at $x^* \approx 3.5$, lying close to the boundary of the recirculation. The free-end shear flow is traced by TKE^* . However, TKE^* in the shear flow is obviously smaller than that in the near wake.

For $Q=1$ (Figs. 8(b), 8(e)), the downwash flow extends further downstream; the maximum streamwise length of the recirculation is $4.1d$. Meanwhile, the maximum TKE^* in the near wake also shifts downstream to $x^* \approx 4.0$. Note that, the maximum TKE^* is 0.15, about 20% smaller compared with the uncontrolled case. A close look at the streamlines over the free end discloses a recirculation bubble formed by the shear flow reattachment under the suction effect (Fig. 8(b)). It is interesting to note that, because of the occurrence of the reattachment, TKE^* over the free end is enhanced significantly compared with the uncontrolled case. The maximum TKE^* in the free-end shear flow is 0.21, about 40% higher than that in the near wake (Fig. 8(e)).

For $Q = 3$ (Fig. 8(c), 8(f)), the flow is fully attached on the free end, suppressing the recirculation on it. The recirculation zone behind the cylinder shrinks a little bit from $Q = 1$, but still larger than the uncontrolled case. Since

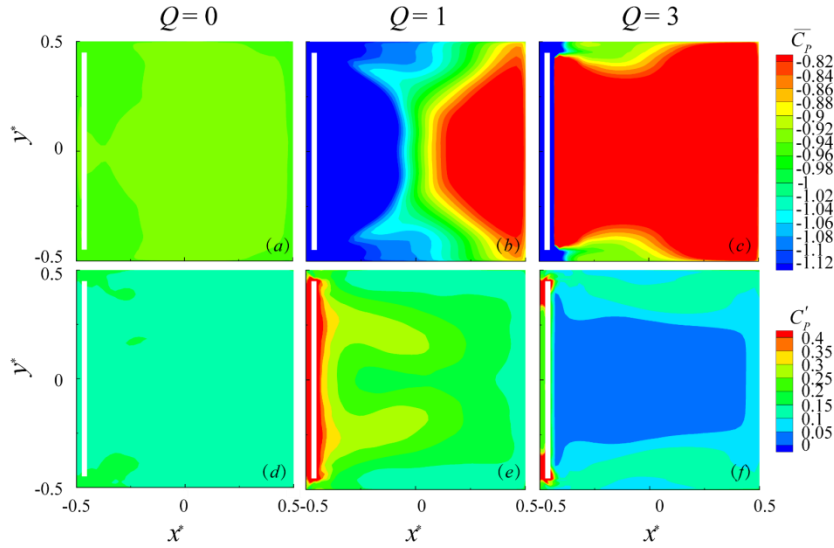


Fig. 7 Distributions of $\overline{C_p}$ and C'_p on the free end

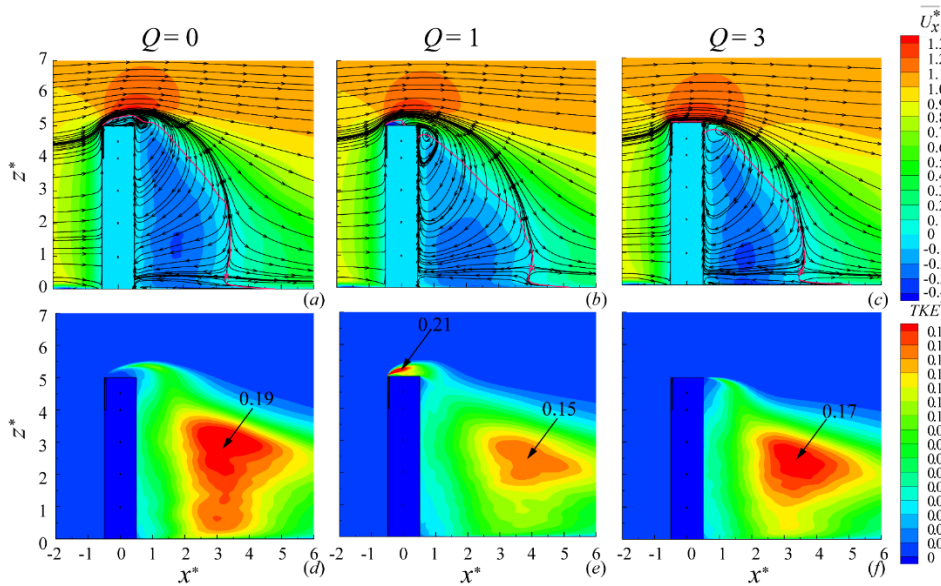


Fig. 8 Time-averaged flow field around the cylinder (a-c) and distributions of TKE^* (d-f) in the central symmetric plane

the flow is fully attached on the free end, the TKE^* over free-end is very small (Fig. 8(e)). Similar to the variation of the recirculation zone, the maximum TKE^* recovers slightly from $Q = 1$, being smaller than that for $Q=0$.

Fig. 9 presents the time-mean streamlines around the free end and the flow visualization results from Wang *et al.* (2018) for $H/d = 5$ and $Re = 3 \times 10^3$. Both streamlines and flow visualization patterns display the same predominant features, though the Reynolds numbers are different for two studies (Fig. 9(a), 9(d)).

For $Q = 1$, according to the smoke flow visualization result (Fig. 9(b)), the free-end shear flow reattaches on the free end. Wang *et al.* (2018), using a Cobra probe, also obtained the velocity distribution over the free end, which confirmed the flow attachment. However, due to the limitations of both Cobra probe and smoke wire technique used by Wang *et al.* (2018), the flow structure in the

recirculation region was not explicitly revealed. In the present LES result (Fig. 9(b)), a source point S appears on the free end. The flow behind point S is attached on the free end pointing downstream, while that upstream of it is reverse. Since point S locates at the central symmetry plane, the divergent flow from point S in the symmetry plane (Fig. 9(b)) indicates the existence of inflow pointing to S from the lateral direction. That is, the flow structure on the free end at $Q = 1$ must be highly three dimensional, which will later be addressed in detail.

With $Q = 3$, the flow on the free end remains fully attached (Fig. 9(c)), consistent with the flow visualization result by Wang *et al.* (2018). Since the flow around the free end is highly 3D, especially at $Q = 1$ (Fig. 9(d)), it is interesting to look into 3D streamlines around the free end, as shown in Fig. 10. The streamlines are colored by the value of mean streamwise velocity $\overline{U_x^*}$. The separation at

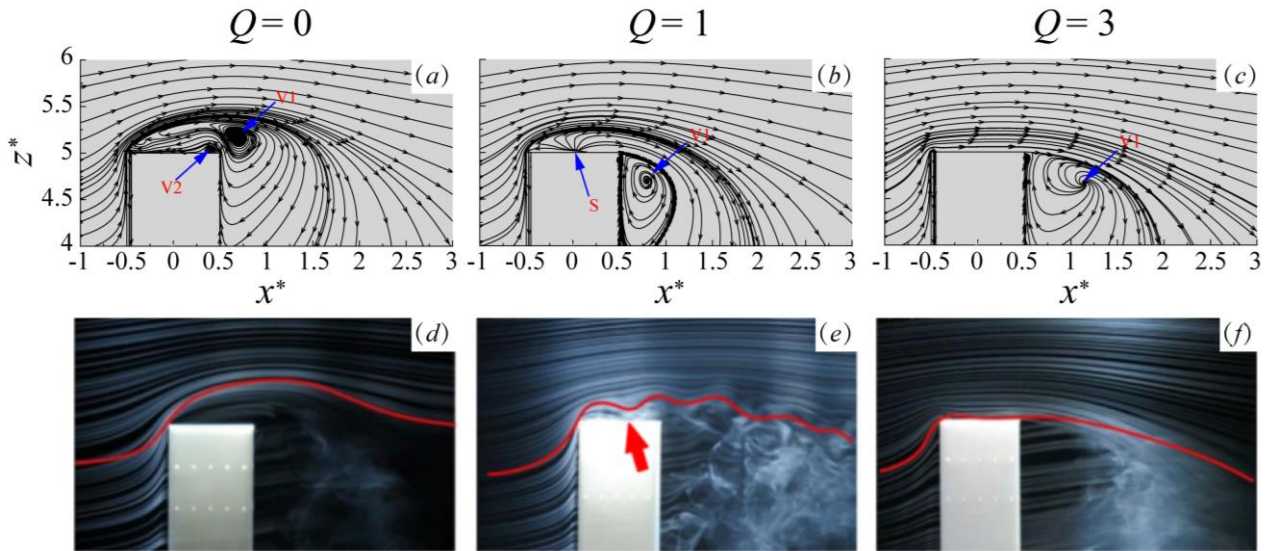


Fig. 9 (a - c) Time-averaged streamlines around the free end in the central symmetric plane at $Re=2.78 \times 10^4$ (present), and (d - f) the corresponding flow visualization results by Wang *et al.* (2018) at $Re = 3 \times 10^3$

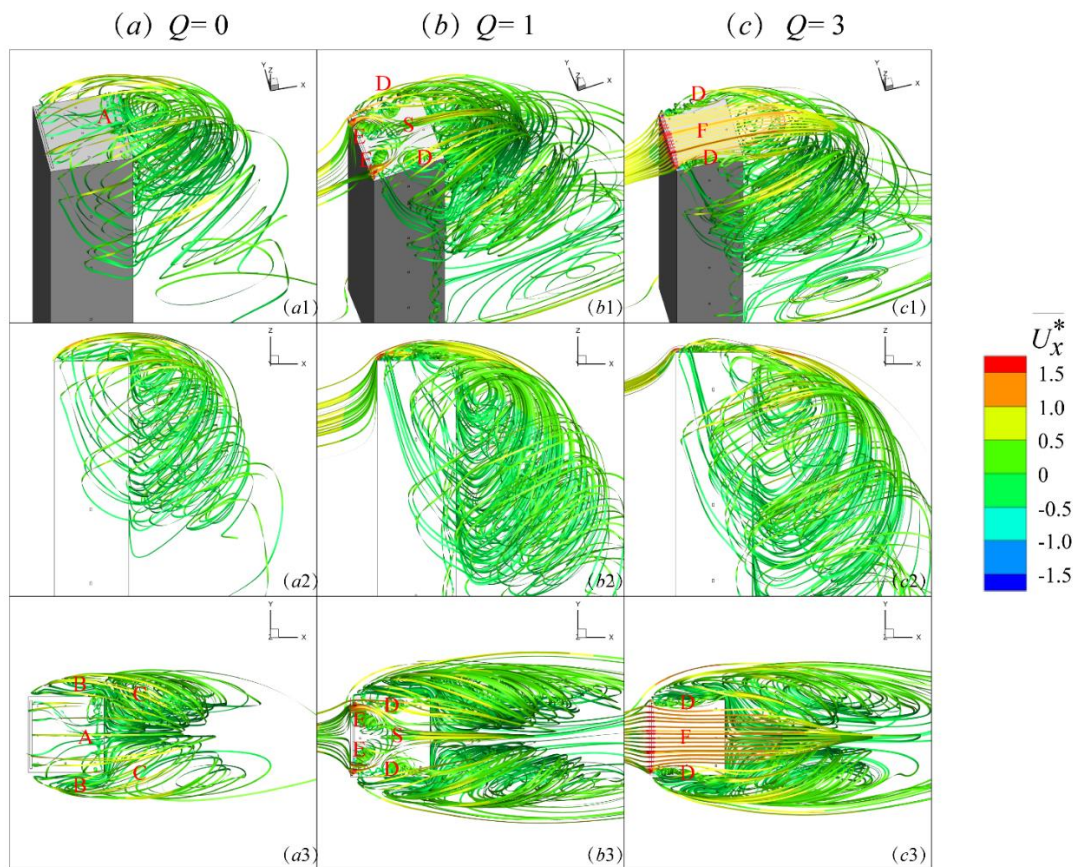


Fig. 10 Time-averaged streamlines around the free end

the free-end leading edge and the secondary vortex at the free-end trailing edge (V2 in Fig. 9(a)) are clearly seen in Fig. 10(a). The acceleration of the free-end shear flow can be also observed, especially in the side view figure. Besides, in Figs. 10(a1) and (a2), an upward flow along the side faces occurs under the entrainment effects of the negative

pressure on the free end (Fig. 7(a)). In Fig. 10(a3), a vortex filament, marked with A, presents near the trailing edge of the free end, which corresponds to the secondary vortex V2 in Fig. 9(a). B and C in Fig. 10(a3) indicate the vortices symmetrically appear at the sides and in the wake, respectively.

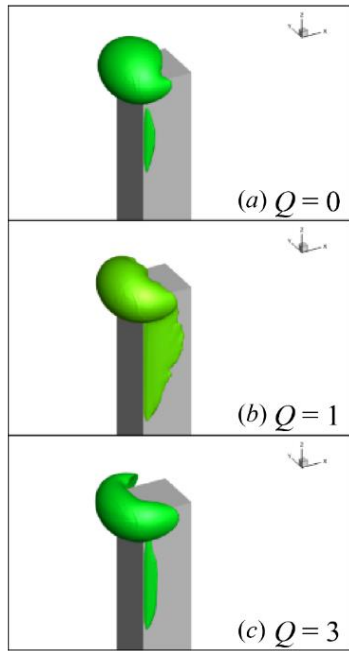


Fig. 11 Iso-surfaces of $\overline{U_z^*}=0.3$ at (a) $Q=0$, (b) $Q=1$, and (c) $Q=3$

When Q is increased to 1, two pairs of vortices appear on the cylinder free end, marked with E and D in Fig. 10(b3). The free-end shear flow is trapped by the suction near the leading edge, forming a pair of strong vortices E, which converge towards the center of the free end. This flow forms a 3D saddle point S on the free end, which essentially corresponds to the source point S in the central symmetric plane, as shown in Fig. 9(b). Taking a close look at the streamlines in Fig. 10(b), it can be found that some upwards flow along the cylinder side faces is driven into vortices E. In addition, another pair of vortices D materializes near the side edges of the free end, mainly formed by the upward flow along the side faces (Figs. 10(b1) and 10(b2)). Both pairs (i.e., E and D) are inherently associated with the highly negative pressure on the cylinder free end (Fig. 7(b)). Moreover, the strong pressure fluctuation on the free end (Fig. 7(e)) can be also ascribed to the violent swirling motion of vortices E and D. It is worth mentioning that, at $Q = 1$, the highly negative pressure on the cylinder free end seems to induce more upward flow along the side faces. This strong upward flow, together with the free-end shear flow, forms the complex 3D flow structures over the free end.

At $Q = 3$, the vortices D yet occurs near the side edges of the free end. However, their size is appreciably small, compared with that at $Q = 1$. Note that the separation at the free-end leading edge is completely suppressed by the suction. The flow is attached on most of the free end, except near the side edges (Fig. 10(c1), (c3)). The observation is also consistent with the flow visualization result by Wang *et al.* (2018).

Since the suction changes the pressure distribution on the free end (Fig. 7), it produces upward flow along the side faces (Fig. 10). Fig. 11 presents the iso-surface of $\overline{U_z^*}=0.3$ for different Q values. This iso-surface traces the area

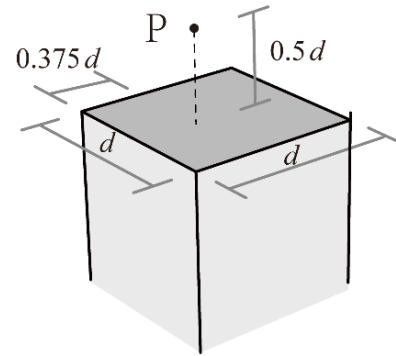


Fig. 12 Sketch showing the position of point P

where the upward flow is relatively strong ($\overline{U_z^*} \geq 0.3$). For $Q = 0$, the upward flow largely appears at the free-end leading edge, which is apparently induced by the ascending free-end shear flow. In addition, a pair of narrow strips appear on the side faces of the cylinder (Fig. 11(a)). At $Q = 1$, the iso-surface near the leading edge shrinks, while that on the side faces enlarges significantly, compared with those at $Q = 0$. At $Q = 3$, the iso-surface near the leading edge shrinks further, which removes the upward free-end shear flow completely. The upward flow area on the side faces also reduces noticeably, compared with that at $Q = 1$.

The upwards flow at the side faces of the cylinder at $Q = 1$ (Fig. 11(b)) is apparently induced by the strong negative pressure on the cylinder free end (Fig. 7(b)). Considering the significant reduction of C_l at $Q = 1$, it is understood that the suction with $Q = 1$ gives rise to the highly 3D vortex structure on the free end (Fig. 10(b)), creating a low pressure on the free end (Fig. 7(b)) and inducing strong upward flows along the side faces of the cylinder (Fig. 11(b)). This upward flows on side faces may weaken the spanwise vortex shedding and thus bring about the reduction in the aerodynamic forces (Figs. 4 and 5).

Recently, Kindree *et al.* (2018) and Peng *et al.* (2019) found that the flow around a WMFLC bears a low-frequency periodicity, with the frequency of about 1/10 of the spanwise Karman vortex shedding. This low-frequency behavior was found to be the up-down flapping of the free-end shear flow, characterizing high- and low-amplitude fluctuations of C_l (Peng *et al.* 2019). We are therefore interested in investigating the dynamic behavior of the free-end shear flow for different Q values.

A point P ($x^* = -0.375$, $y^* = 0$ and $z^* = 5.5$, $0.5d$ above the free end, as shown in figure 12) is selected to monitor the behavior of the free end shear flow. Figure 13 presents the time histories of the velocities (U_y^* and U_z^*) in the lateral and vertical directions. The corresponding C_l is also shown for a comparison purpose. As discussed in figure 5, C_l changes alternately from the high- to low-amplitude fluctuations, as also observed by Bourgeois *et al.* (2011), Sattari *et al.* (2012), Uffinger *et al.* (2013) and Wang *et al.* (2018), etc. Peng *et al.* (2019) suggested that the high- and low-amplitude lift forces are associated with the change in the spanwise vortex shedding from asymmetrical to symmetrical modes and also with the flapping of the free-end shear flow. As seen in Fig. 13(a), a low-frequency

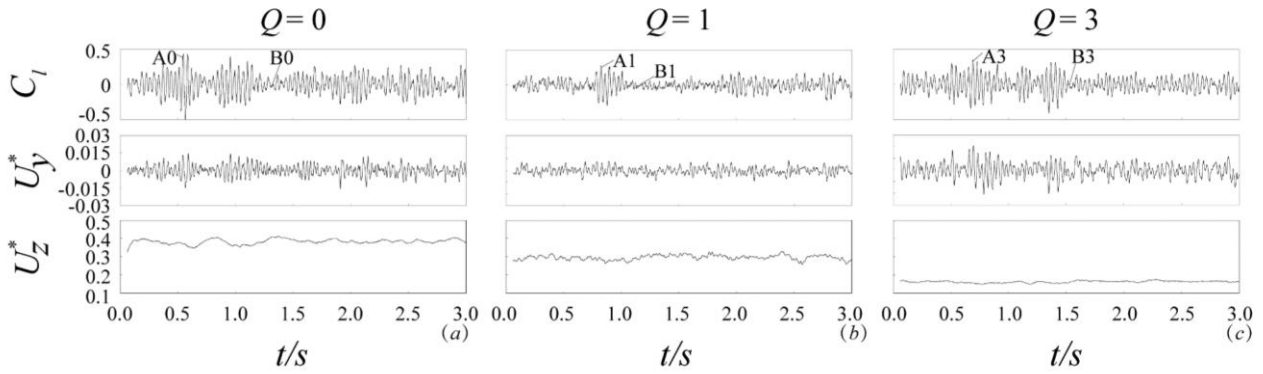


Fig. 13 Time-histories of U_y^* and U_z^* at point P together with C_l for (a) $Q = 0$, (b) $Q = 1$, and (c) $Q = 3$

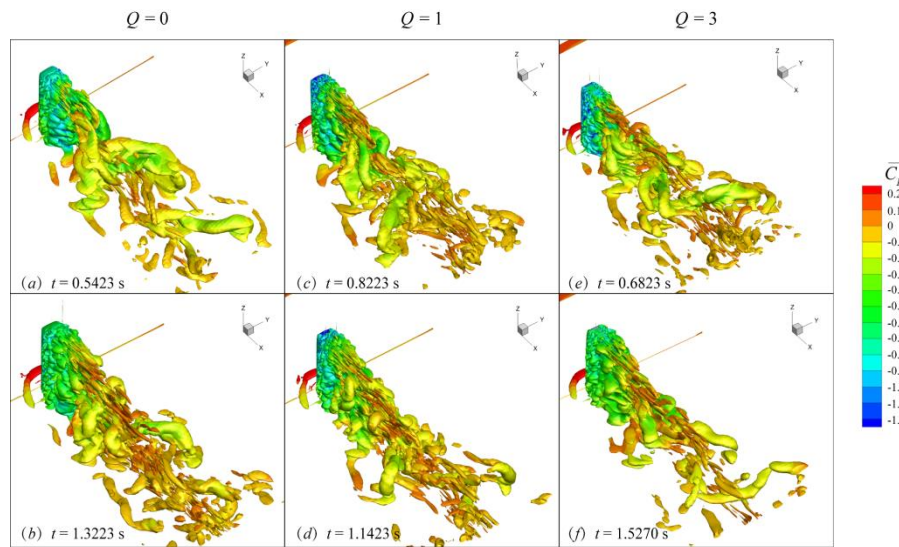


Fig. 14 Instantaneous near wake structures with $\lambda_2 = 0.6$: (a, b) $Q = 0$, (c, d) $Q = 1$, and (e, f) $Q = 3$

variation in U_z^* is clearly observed, indicating the up-down flapping of the free-end shear flow. This low-frequency flapping of the free-end shear flow causes the fluctuations in C_l and U_y^* , the latter is associated with the spanwise vortex shedding modes. Note that, the averaged U_z^* is about 0.38 at $Q = 0$, suggesting the free-end shear flow bends upward at point P. This observation is consistent with the flow visualization results by Wang *et al.* (2018), as shown in Fig. 9(a).

At $Q = 1$, the averaged U_z^* reduces to about 0.28 (Fig. 13(b)), smaller than that at $Q = 0$ (Fig. 13(a)), suggesting that the shear flow is restricted closer to the free end by the slot suction. As shown in Fig. 13(b), the low-frequency variation in U_z^* is less obvious compared to the uncontrolled case. Meanwhile, the occurrence of the high-amplitude fluctuation in C_l is also significantly suppressed. That is, the free-end shear flow still flaps, albeit weakly, which sparks the C_l fluctuation.

At $Q = 3$, the low-frequency modulation in U_z^* disappears (Fig. 13(c)), with the averaged U_z^* reducing to about 0.16. Given that the shear flow is fully attached on the free end (Fig. 9(c)), the low-frequency flapping of the free-end shear flow completely ceases. Although the

flapping disappears, the occurrences of high- and low-amplitude fluctuation of C_l are still discernible again, suggesting a weak or no correlation between the free-end shear flow flapping and the spanwise vortex shedding (Peng *et al.* 2019) when the shear flow is fully attached.

3.2.2 Near wake

For all the cases tested, two typical instants A and B are selected corresponding to high- and low-amplitude C_l , respectively (Fig. 13). The corresponding near wake flow structures at instants A and B are compared in Fig. 14, where the iso-surfaces of λ_2 (Zhang *et al.* 2017) are colored by pressure coefficient C_p . The λ_2 is defined as

$$\lambda_2 = 0.5(r_{ij}r_{ij} - s_{ij}s_{ij}) \quad , \quad \text{with} \quad r_{ij} = 0.5\left(\frac{\partial u_i}{\partial x_j} - \frac{\partial u_j}{\partial x_i}\right) \quad \text{and}$$

$$s_{ij} = 0.5\left(\frac{\partial u_i}{\partial x_j} + \frac{\partial u_j}{\partial x_i}\right) \quad \text{being the symmetrical strain tensor}$$

and skew-symmetrical rotation tensor, respectively.

For $Q = 0$, the two typical vortex shedding modes are clearly observed (Figs. 14(a), 14(b)). The near wake presents alternating vortex shedding for high-amplitude C_l

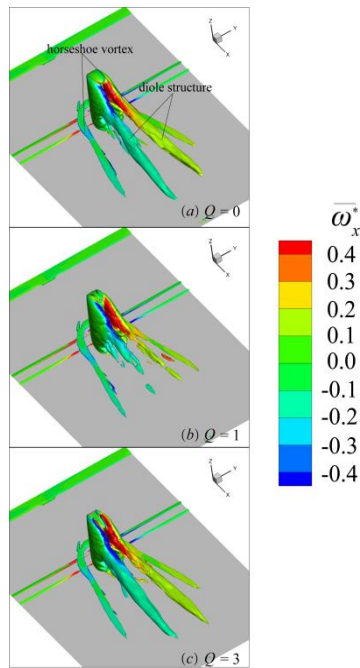


Fig. 15 Time-average near wake structures with $\lambda_2 = 0.4$: (a) $Q = 0$, (b) $Q = 1$, and (c) $Q = 3$

(Fig. 14(a)) while a symmetric shedding persists for the low-amplitude C_l (Fig. 14(b)). As such, the wake is narrower in the latter case than in the former. When the free-end suction applied, the alternating vortices are less organized, breaking into random small-scale vortices, especially for $Q=1$. The wake is still wide for the high-amplitude C_l and narrow for the high-amplitude C_l (Figs. 14(c) - 14(f)).

Fig. 15 compares the time-mean near wake structure for the three tested cases. Besides the horseshoe vortices on the ground wall, a clear dipole structure features the wake for $Q=0$ (Porteous *et al.* 2017). The absence of base vortex can be ascribed to the small boundary layer thickness used in the present investigation (Wang *et al.* 2006). For $Q=1$, the dipole structure is impaired, compared with that for $Q=0$. The tip vortex is enhanced again for $Q=3$, which is consistent with the dependence of the aerodynamic forces on Q .

4. Conclusions

The mechanism of force and flow control by a steady slot suction near the free-end leading edge of a wall-mounted finite-length square cylinder is numerically investigated. Three suction ratios $Q=0, 1$, and 3 are tested to reveal the effect of Q on the near wake and aerodynamic forces. The results lead to the following conclusions:

- The maximal reduction of aerodynamic forces occurs at $Q=1$. The maximum reduction in time-mean drag, fluctuating drag, and fluctuating lift are 3.75%, 19.08%, and 40.91%, respectively, compared to the uncontrolled case ($Q=0$). The $Q=3$ offers larger and smaller forces than $Q=1$ and 0 , respectively.
- At $Q=1$, two pairs of vortices appear on the free end,

resulting in a very low-pressure region at the upstream half of the free end. This low pressure drives a strong upward moving flow along the side faces of the cylinder, which weakens the spanwise vortex shedding. The TKE in the free-end shear flow is the strongest, enhancing the momentum transport between the free-end shear flow and near wake. While partially attached in the free-end surface for $Q=1$, the free-end shear flow is fully attached for $Q=3$ and fully detached or $Q=0$. The fully attached flow for $Q=3$ enhances the pressure on the free end and weakens the induced upward moving flow along the side faces.

- As the boundary layer thickness is quite small, only tip vortices appear in the near wake for all the cases. Particularly, for $Q=1$, the time-mean tip vortices are dramatically impaired, and the alternating spanwise vortex shedding weakens. When Q is increased to 3 , the tip vortices and alternating vortex shedding both are reinforced.

References

- Alam, M.M., Zhou, Y., Zhao, J.M., Flamand O. and Boujard, O. (2010), "Classification of the tripped cylinder wake and bi-stable phenomenon", *Int. J. Heat Fluid Flow*, **31**(4), 545-560. <https://doi.org/10.1016/j.ijheatfluidflow.2010.02.018>.
- Bai, H.L. and Alam, M.M. (2018), "Dependence of square cylinder wake on Reynolds Number", *Phys. Fluids*, **30**, 015102, 1-19. <https://doi.org/10.1063/1.4996945>.
- Bhatt, R. and Alam, M.M. (2018), "Vibration of a square cylinder submerged in a wake", *J. Fluid Mech.*, **853**, 301-332. <https://doi.org/10.1017/jfm.2018.573>.
- Bourgeois, J.A., Noack, B.R. and Martinuzzi, R.J. (2013), "Generalized phase average with applications to sensor-based flow estimation of the wall-mounted square cylinder wake", *J. Fluid Mech.*, **736**, 316-350. <https://doi.org/10.1017/jfm.2013.494>.
- Bourgeois, J.A., Sattari, P. and Martinuzzi, R.J. (2011), "Alternating half-loop shedding in the turbulent wake of a finite surface-mounted square cylinder with a thin boundary layer", *Phys. Fluids*, **23**(9), 95101. <https://doi.org/10.1063/1.3623463>.
- Bourgeois, J.A., Sattari, P. and Martinuzzi, R.J. (2012), "Coherent vortical and straining structures in the finite wall-mounted square cylinder", *Int. J. Heat Fluid Flow*, **35**, 130-140. <https://doi.org/10.1016/j.ijheatfluidflow.2012.01.009>.
- Cao, Y., Tamura, T. and Kawai, H. (2019), "Investigation of wall pressures and surface flow patterns on a wall-mounted square cylinder using very high-resolution Cartesian mesh", *J. Wind Eng. Ind. Aerod.*, **188**, 1-18. <https://doi.org/10.1016/j.jweia.2019.02.013>.
- Carassale, L., Freda, A. and Michela, M.B. (2014), "Experimental investigation on the aerodynamic behavior of square cylinders with rounded corners", *J. Fluids Struct.*, **44**, 195-204. <https://doi.org/10.1016/j.jfluidstructs.2013.10.010>.
- Chen, H.L., Dai, S.S., Jia, L. and Yao, X.L. (2009), "Three-dimensional numerical simulation of the flow past a circular cylinder based on LES method", *J. Marine Sci. Appl.*, **8**(2), 110-116. <https://doi.org/10.1007/s11804-009-8110-4>.
- Choi, H.C., Jeon, W.P. and Kim, J.S. (2008), "Control of flow over a bluff body", *Annu. Rev. Fluid Mech.*, **40**, 113-139. <https://doi.org/10.1146/annurev.fluid.39.050905.110149>.
- Derakhshandeh, J.F. and Alam, M.M. (2019), "A review of bluff body wakes", *Ocean Eng.*, **182**, 475-488.
- Dutton, R. (1990), "Reduction of tall building motion by

- aerodynamic treatments”, *J. Wind Eng. Ind. Aerod.*, **36**(Part 2), 739-744. [https://doi.org/10.1016/0167-6105\(90\)90071-J](https://doi.org/10.1016/0167-6105(90)90071-J).
- Gu, M. and Quan, Y. (2004), “Across-wind loads of typical tall buildings”, *J. Wind Eng. Ind. Aerod.*, **92**, 1147-1165. <https://doi.org/10.1016/j.jweia.2004.06.004>.
- Kawai, H. (1998), “Effect of corner modifications on aeroelastic instabilities of tall buildings”, *J. Wind Eng. Ind. Aerod.*, **74-76**(1), 719-729. [https://doi.org/10.1016/S0167-6105\(98\)00065-8](https://doi.org/10.1016/S0167-6105(98)00065-8).
- Kawai, H., Okuda, Y. and Ohashi, M. (2012), “Near wake structure behind a 3D square prism with the aspect ratio of 2.7 in a shallow boundary layer flow”, *J. Wind Eng. Ind. Aerod.*, **104-106**, 196-202. <https://doi.org/10.1016/j.jweia.2012.04.019>.
- Kim, Y.C., Bandi, E.K., Yoshida, A. and Tamura, Y. (2015), “Response characteristics of super-tall buildings - Effects of number of sides and helical angle”, *J. Wind Eng. Ind. Aerod.*, **145**, 252-262. <https://doi.org/10.1016/j.jweia.2015.07.001>.
- Kindree, M.G., Shahroodi, M. and Martinuzzi, R.J. (2018) “Low-frequency dynamics in the turbulent wake of cantilevered square and circular cylinders protruding a thin laminar boundary layer”, *Experim. Fluids*, **59**, 186. <https://doi.org/10.1007/s00348-018-2641-x>.
- Kotapati, R.B., Mittal, R. and Cattafesta Iii, L.N. (2007), “Numerical study of a transitional synthetic jet in quiescent external flow”, *J. Fluid Mech.*, **581**, 287-231.
- Krajnovic, S. (2011), “Flow around a tall finite cylinder explored by large eddy simulation”, *J. Fluid Mech.*, **676**(10), 294-317. <https://doi.org/10.1017/S0022112011000450>.
- Krajnovic, S. and Davidson L. (2002), “Large-Eddy Simulation of the flow around a bluff body”, *ALAA J.*, **40**(5), 927-936. <https://doi.org/10.2514/2.1729>.
- Lee, B.E. (1975), “The effect of turbulence on the surface pressure field of a square prism”, *J. Fluid Mech.*, **69**(2), 263-282. <https://doi.org/10.1017/S0022112075001437>.
- Li, Y., Xiang, T., Kong, F.T., Qiu, S. L. and Yong, G.L. (2018), “Aerodynamic treatments for reduction of wind loads on high-rise buildings”, *J. Wind Eng. Ind. Aerod.*, **172**, 107-115. <https://doi.org/10.1016/j.jweia.2017.11.006>.
- Li, Z.J., Navon, I.M., Hussaini, M.Y. and Le Dimet, F.X. (2003), “Optimal control of cylinder wakes via suction and blowing”, *Comput. Fluids*, **32**(2), 149-171. [https://doi.org/10.1016/S0045-7930\(02\)00007-5](https://doi.org/10.1016/S0045-7930(02)00007-5).
- Lilly, D.K. (1992), “A proposed modification of the Germano subgrid-scale closure method”, *Phys. Fluids*, **4**(3), 633-635. <https://doi.org/10.1063/1.858280>.
- McClellan, J.F. and Sumner, D. (2014), “An experimental investigation of aspect ratio and incidence angle effects for the flow around surface-mounted finite-height square prisms”, *J. Fluids Eng.*, **136**(8), 081206. <https://doi.org/10.1115/1.4027138>.
- Menicovich, D., Lander, D., Vollen, J., Amitay, M., Letchford, C. and Dyson, A. (2014), “Improving aerodynamic performance of tall buildings using Fluid based Aerodynamic Modification”, *J. Wind Eng. Ind. Aerod.*, **133**, 263-273. <https://doi.org/10.1016/j.jweia.2014.08.011>.
- Mooneghi, M.A. and Kargarmoakhar, R. (2016) “Aerodynamic mitigation and shape optimization of buildings: Review”, *J. Build. Eng.*, **6**, 225-235. <https://doi.org/10.1016/j.jobe.2016.01.009>.
- Noda, H. and Nakayama, A. (2003), “Free-stream turbulence effects on the instantaneous pressure and forces on cylinders of rectangular cross section”, *Experim. Fluids*, **34**, 332-344. <https://doi.org/10.1007/s00348-002-0562-0>.
- Okamoto, S. and Sunabashiri, Y. (1992), “Vortex shedding from a circular cylinder of finite length placed on a ground plane”, *J. Fluids Eng.*, **114**(4), 512-521. <https://doi.org/10.1115/1.2910062>.
- Park, C.W. and Lee, S.J. (2000), “Free end effects on the near wake flow structure behind a finite circular cylinder”, *J. Wind Eng. Ind. Aerod.*, **88**, 231-246. [https://doi.org/10.1016/S0167-6105\(00\)00051-9](https://doi.org/10.1016/S0167-6105(00)00051-9).
- Park, C.W. and Lee, S.J. (2004), “Effects of free-end corner shape on flow structure around a finite cylinder”. *J. Fluids Struct.*, **19**(2), 141-158. <https://doi.org/10.1016/j.jfluidstructs.2003.12.001>.
- Pattenden, R.J., Turnock, S.R. and Zhang, X. (2005), “Measurements of the flow over a low-aspect-ratio cylinder mounted on a ground plane”, *Experim. Fluids*, **39**, 10-21. <https://doi.org/10.1007/s00348-005-0949-9>.
- Peng, S., Wang, H.F., Zeng, L.W. and He, X.H. (2019), “Low-frequency dynamics of the flow around a finite-length square cylinder”, *Experim. Therm. Fluid Sci.*, **109**, 109877. <https://doi.org/10.1016/j.expthermflusci.2019.109877>.
- Porteous, R., Moreau, D.J. and Doolan, C.J. (2014), “A review of flow induced noise from finite wall-mounted cylinders”, *J. Fluids Struct.*, **51**, 240-254. <https://doi.org/10.1016/j.jfluidstructs.2014.08.012>.
- Porteous, R., Moreau, D.J. and Doolan, C.J. (2017), “The aeroacoustics of finite wall-mounted square cylinders”, *J. Fluid Mech.*, **832**(10), 287-328. <https://doi.org/10.1017/jfm.2017.682>.
- Quan, Y. and Gu, M. (2012), “Across-wind equivalent static wind loads and responses of super-high-rise buildings”, *Advan. Struct. Eng.*, **15**(12), 2145-2155. <https://doi.org/10.1260/2F1369-4332.15.12.2145>.
- Rastan, M.R., Sohankar, A. and Alam, M.M. (2017), “Low-Reynolds-number flow around a wall-mounted square cylinder: Flow structures and onset of vortex shedding”, *Phys. Fluids*, **29**, 103601. <https://doi.org/10.1063/1.4989745>.
- Rastan, M.R., Sohankar, A., Doolan, C., Moreau, D., Shirani, E. and Alam, M.M. (2019), “Controlled flow over a finite square cylinder using suction and blowing”, *Int. J. Mech. Sci.*, **156**, 410-434. <https://doi.org/10.1016/j.ijmecsci.2019.04.013>.
- Saeedi, M., Lepoudre, P.P. and Wang, B.C. (2014), “Direct numerical simulation of turbulent wake behind a surface-mounted square cylinder”, *J. Fluids Struct.*, **51**, 20-39. <https://doi.org/10.1016/j.jfluidstructs.2014.06.021>.
- Saha, A.K. (2013), “Unsteady flow past a finite square cylinder mounted on a wall at low Reynolds number”, *Comput. Fluids*, **88**(15), 599-615. <https://doi.org/10.1016/j.compfluid.2013.10.010>.
- Sakamoto, H. (1985), “Aerodynamic forces acting on a rectangular prism placed vertically in a turbulent boundary layer”, *J. Wind Eng. Ind. Aerod.*, **18**(2), 131-151. [https://doi.org/10.1016/0167-6105\(85\)90093-5](https://doi.org/10.1016/0167-6105(85)90093-5).
- Sakamoto, H. and Mikio, A. (1983), “Vortex shedding from a rectangular prism and a circular cylinder placed vertically in a turbulent boundary layer”, *J. Fluid Mech.*, **126**, 147-165. <https://doi.org/10.1017/S0022112083000087>.
- Sakamoto, H. and Oiwake, S. (1984), “Fluctuating forces on a rectangular prism and a circular cylinder placed vertically in a turbulent boundary layer”, *J. Wind Eng. Ind. Aerody.*, **106**(2), 160-166. <https://doi.org/10.1115/1.3243093>.
- Sattari, P., Bourgeois, J.A. and Martinuzzi, R.J. (2012), “On the vortex dynamics in the wake of a finite surface-mounted square cylinder”, *Experim. Fluids*, **52**(5), 1149-1167. <https://doi.org/10.1007/s00348-011-1244-6>.
- Shang, J., Zhou, Q., Alam, M.M., Liao, H. and Cao, S. (2019), “Numerical study of the flow structure and aerodynamic forces on two tandem square cylinders with different chamfered-corner ratio”, *Phys. Fluids*, **31**, 075102, 1-15. <https://doi.org/10.1063/1.5100266>.
- Smagorinsky, J. (1963), “General circulation experiments with the primitive equations”, *Mon. Weather Rev.*, **91**(3), 99-164. [https://doi.org/10.1175/1520-0493\(1963\)091%3C0099:GCEWTP%3E2.3.CO;2](https://doi.org/10.1175/1520-0493(1963)091%3C0099:GCEWTP%3E2.3.CO;2).

- Sohankar, A., Abbasi, M. Nili-Ahmadabai, M., Alam, M.M. and Zafar, F. (2018a), "Experimental study of the flow around two finite square cylinders", *Arch. Mech.*, **70**, 457- 480.
- Sohankar, A., Esfeh, M., Pourjafan, H., Alam, M.M. and Wang, L. (2018b), "Features of the flow over a finite length square prism on a wall at various incidence angles", *Wind Struct.*, **26**(5), 317-329. <https://doi.org/10.12989/was.2018.26.5.317>.
- Sumner, A. and Ogunremi, A. (2015), "On the effects of incidence angle on the mean wake of a surface-mounted finite-height square prism", *In Proceedings of the ASME-JSME-KSME.*, July.
- Sumner, D., Heseltine, J.L., Dansereau, O. and Dansereau, J.P. (2004), "Wake structure of a finite circular cylinder of small aspect ratio", *Experim. Fluids*, **37**(5), 720-730. <https://doi.org/10.1007/s00348-004-0862-7>.
- Sumner, D., Rostamy, N., Bergstrom, D.J. and Bugg, J.D. (2017), "Influence of aspect ratio on the mean flow field of a surface-mounted finite-height square prism", *Int. J. Heat Fluid Flow*, **65**, 1-20. <https://doi.org/10.1016/j.ijheatfluidflow.2017.02.004>.
- Tanaka, H., Tamura, Y., Ohtake, K., Nakai, M. and Kim, Y.C. (2012), "Experimental investigation of aerodynamic forces and wind pressures acting on tall buildings with various unconventional configurations", *J. Wind Eng. Ind. Aerod.*, **107-108**, 179-191. <https://doi.org/10.1016/j.jweia.2012.04.014>.
- Tanaka, S. and Murata, S. (1999), "An investigation of the wake structure and aerodynamic characteristics of a finite Circular Cylinder", *JSME Int. J. Series B: Fluids Therm. Eng.*, **42**(2), 178-187. <https://doi.org/10.1299/jsmeb.42.178>.
- Tutar, M., Hold, A.E. and Lewis, A.P. (1998), "Comparative performance of various two equation models and LES on simulated flow past a circular cylinder in subcritical flow regime", *The Proceedings of ASME Fluids Engineering Summer Meeting on Finite Element Application in Fluid Dynamics*, Washington, D.C., USA.
- Uffinger, T., Ali, I. and Becker, S. (2013). "Experimental and numerical investigations of the flow around three different wall-mounted cylinder geometries of finite length", *J. Wind Eng. Ind. Aerod.*, **119**, 13-27. <https://doi.org/10.1016/j.jweia.2013.05.006>.
- Unnikrishnan, S. and Ogunremi, A. (2017), "The effect of incidence angle on the mean wake of surface-mounted finite-height square prisms", *Int. J. Heat Fluid Flow*, **66**, 137-156. <https://doi.org/10.1016/j.ijheatfluidflow.2017.05.012>.
- Wang, H.F. and Zhou, Y. (2009), "The finite length square cylinder near wake", *J. Fluid Mech.*, **638**(10), 453-490. <https://doi.org/10.1017/S0022112009990693>.
- Wang, H.F., Peng, S., Li, Y. and He X.H. (2018), "Control of the aerodynamic forces of a finite-length square cylinder with steady slot suction at its free end", *J. Wind Eng. Ind. Aerod.*, **179**, 438-448. <https://doi.org/10.1016/j.jweia.2018.06.016>.
- Wang, H.F., Peng, S., Zhou, Y. and He, X.H. (2016), "Transition along a finite-length cylinder in the presence of a thin boundary layer", *Experim. Fluids*, **57**(5), 1-10. <https://doi.org/10.1007/s00348-016-2160-6>.
- Wang, H.F., Zhao, X.Y., He, X.H. and Zhou, Y. (2017), "Effects of oncoming flow conditions on the aerodynamic forces on a cantilevered square cylinder", *J. Fluid Struct.*, **75**, 140-157. <https://doi.org/10.1016/j.jfluidstructs.2017.09.004>.
- Wang, H.F., Zhou, Y., Chan, C.K. and Lam, K.S. (2006), "Effect of initial conditions on interaction between a boundary layer and a wall-mounted finite-length-cylinder wake", *Phys. Fluids*, **18**(6), 065106. <https://doi.org/10.1063/1.2212329>.
- Xie, J.M. (2014), "Aerodynamic optimization of super-tall buildings and its effectiveness assessment", *J. Wind Eng. Ind. Aerod.*, **130**, 88-98. <https://doi.org/10.1016/j.jweia.2014.04.004>.
- Zafar, F. and Alam, M.M. (2019), "Flow structure and heat transfer from cylinders modified from square to circular", *Phys. Fluids*, **31**(8), 083604. <https://doi.org/10.1063/1.5109693>.
- Zhang, D., Cheng, L., An, H.W. and Zhao, M. (2017), "Direct numerical simulation of flow around a surface-mounted finite square cylinder at low Reynolds numbers", *Phys. Fluids*, **29**(4), 045101. <https://doi.org/10.1063/1.4979479>.
- Zhang, H., Xin, D. and Ou, J. (2016), "Steady suction for controlling across-wind loading of high-rise buildings", *Struct. Design Tall Spec. Build.*, **25**(15), 785-800. <https://doi.org/10.1002/tal.1283>.
- Zheng, C.R. and Zhang, Y.C. (2012), "Computational fluid dynamics study on performance and mechanism of suction control over a high-rise building", *Struct. Design Tall Spec. Build.*, **21**(7), 475-491. <https://doi.org/10.1002/tal.622>.
- Zheng, Q. and Alam, M.M. (2017), "Intrinsic features of flow past three square prisms in side-by-side arrangement", *J. Fluid Mech.*, **826**, 996-1033. <https://doi.org/10.1017/jfm.2017.378>.

AM